Modelling of an intersubband quantum confined Stark effect in Ge quantum wells for mid-infrared photonics

A. BARZAGHI,[1] V. FALCONE,[1] S. CALCATERRA,[1] D. MARRIS-MORINI,[2] M. VIRGILIO,[3] AND J. FRIGERIO[1,*]

[1]*L-NESS, Dipartimento di Fisica, Politecnico di Milano, 20133 Milano, Italy*
[2]*Centre de Nanosciences et de Nanotechnologies, Université Paris-Saclay, CNRS, 91120 Palaiseau, France*
[3]*Dipartimento di Fisica "E. Fermi", Università di Pisa, Largo Pontecorvo 3, I-56127 Pisa, Italy*
[*]*jacopo.frigerio@polimi.it*

Abstract: In this work we theoretically investigate quantum confined Stark effect of intersubband transitions in asymmetric Ge/SiGe quantum wells for intensity modulation in the mid-infrared. Our calculations show that extinction ratios up to 1 dB and modulation speeds of several tens of GHz could be obtained in 100 μm long waveguides.

Introduction

Photonic integrated circuits (PICs) operating in the Mid- infrared (MIR) are receiving increasing attention due to the variety of envisaged applications in medical diagnostics [1], analytical chemistry [2], environmental monitoring [3], and sensing for safety and security [4]. In the MIR molecules feature unique, spectrally narrow vibrational bands. Therefore, the innovation brought by MIR PIC sensors, compared to their visible (VIS) and near-infrared (NIR) counterparts, consists in the detection of such unique "spectral fingerprints", instead of the less specific refractive index change in the VIS/NIR. The recent commercial availability of compact wavelength-tunable quantum cascade lasers (QCLs) in the MIR range from 4 to 14 μm [5] has enabled, in recent years, the design and the realization of automated MIR molecular sensors with high molecule specificity in a label-free approach [6]. Key applications include the atmospheric sensing of carbon dioxide and monoxide (and toxic gases in general), the identification of cancer biomarkers through the analysis of the amide bands of proteins, and the quantification of glucose, aldehydes, alcohols in blood or saliva for rapid health monitoring. In this framework, the development of integrated electro-optic modulators (EOM) is of high interest for sensitivity enhancement via synchronous detection [7]. In addition, the presence of two atmospheric transmission windows in the MIR (3-5 μm and 8-14 μm [8]) makes the development of high-speed EOM appealing for free space optical communications [6,9].

Silicon-on-insulator (SOI) modulators relying on free carrier plasma dispersion (FCPD) have been widely developed for telecom wavelengths and their operation has been recently extended up to 3.8 μm [10,11], nevertheless the use of this platform at longer wavelengths is hindered by the strong absorption of SiO2 beyond 4 μm. Ge and Ge-rich SiGe alloys are very promising material platforms for the long-wave infrared (LWIR), thanks to their broad transparency range (up to λ = 15 μm for pure Ge). The compelling opportunities offered by these materials have stimulated intense research efforts, resulting in the demonstration of many photonics building blocks [11–19]. Nevertheless, electro-optic modulation at LWIR wavelengths is still in its infancy. EOM based on FCPD has been recently demonstrated in Ge-on-Si [20] and SiGe-on-Si [21,22] platforms operating between 3.8-8 μm and 6.4-10.7 μm respectively. The main drawback observed in such works is the long propagation length (typically few mm) necessary to achieve extinction

ratios higher than 1 dB. Such long devices feature large associated capacitances, which limit the modulation speed to a few hundreds of MHz [21].

An alternative approach to achieve efficient electro-optic modulation at LWIR wavelengths is to leverage on the variation of the absorption spectrum induced by the Quantum Confined Stark Effect (QCSE) in semiconductor quantum wells (QW). The QCSE is related to the application of an electric field in the direction normal to the QW plane, which influences the spatial distribution of the wavefunction of electrons and holes confined in the wells, as well as the energy of the related quantum states. QCSE based modulators are an established technology at telecom wavelengths both with III-V [23] and group-IV [24] based QWs. At such wavelengths the QCSE modulation of the absorption spectrum is related to the tuning of inter-band transitions involving confined states in the valence band (CB) and in the conduction band (VB) of intrinsic QW systems. In particular electrically biasing the QW the electron states shift to lower energies, while the hole states shift to higher energies, causing a red-shift of the absorption spectrum. Additionally, the external electric field shifts electrons and holes to opposite sides of the well, decreasing their wavefunction overlap integral, which in turn reduces the exciton-based absorption. At mid-infrared frequencies, the QCSE modulation is instead related to inter-subband transitions (IST) within the CB or the VB in n- and p-type devices, respectively. In a symmetric quantum well, the external electric field would cause similar effects on all the quantum states belonging to the same band, so, in order to enhance the inter-subband QCSE, QWs with asymmetric potential profiles are required.

Proof-of-concept demonstrations of high-speed intensity modulation relying of this kind of approach have been reported in free space configuration only, using III-V materials [25]. To move a step forward in this direction, here we present a numerical study suggesting the feasibility of an electro-optic modulation based on the inter-subband QCSE in waveguide-integrated p-type Ge/SiGe asymmetric QWs. We focus on the SiGe material system to benefit from its prompt compatibility with standard Si foundry processes. The choice of a hole base device is motivated by the larger offsets, occurring in the valence band of Ge/SiGe QWs with respect to the conduction one. More precisely valence band discontinuities can easily reach values up to 0.3 eV, as required to design IST falling in the mid-infrared spectral range, as for instance shown in [26,27] where intersubband optical absorption in this spectral range is reported or in [28,29] where p-type Ge/SiGe asymmetric QW has been used to demonstrate giant MIR second harmonic generation.

Theoretical data here presented indicate that Ge/SiGe QWs with stepped and triangular potential profiles could be exploited to obtain high-speed modulation at mid-infrared frequencies, with extinction ratios higher than 1 dB in 100-μm long waveguides and modulation speeds of several tens of GHz.

Electronic structure and optical absorption modelling

Two different asymmetric QW profiles have been investigated in this work: a stepped quantum well (StQW) and a triangular quantum well (TQW), whose schemes are reported in Fig. 1 (a) and (b) respectively. The StQW period consists of a 6 nm thick $Si_{0.35}Ge_{65}$ barrier followed by the 3 nm Ge main well (p-doped with a density of 1×10^{18} cm^{-3}) and a 6 nm intrinsic $Si_{0.3}Ge_{0.7}$ layer, acting as step well. The heterostructure is designed to achieve strain symmetrisation (the compressive strain in the wells is compensated by the tensile strain in the barriers), with an in-plane lattice parameter set by the relaxed (i.e. cubic) $Si_{0.2}Ge_{0.8}$ virtual substrate (VS). The TQW period consists of a 4.5 nm thick $Si_{0.5}Ge_{0.5}$ barrier followed by a 2 nm Ge well (hole doped with a density of 1×10^{18} cm^{-3}) and a graded barrier whose Ge concentration x decreases linearly from 1 to 0.5 in 6 nm. Also in this case the QW layers are strain symmetrized and have an in-plane lattice parameter set by the cubic $Si_{0.3}Ge_{0.7}$ VS. The fine control of the thicknesses and compositions required to realize such heterostructures are well within the capabilities of the SiGe epitaxial deposition technology [29,30].
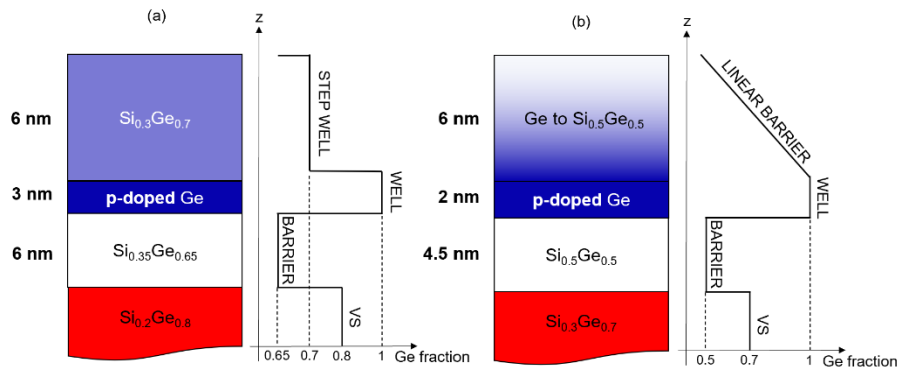
Fig. 1. Schematics of the StQW (a) and of the TQW (b) structures together with the Ge concentration profile of the multilayer stack.

As a first step, we calculated the electronic band structure using a semi-empirical first-neighbor tight-binding Hamiltonian which includes spin-orbit interaction (see Ref. [31,32] for details on the model). Thanks to this multi-orbital description, all the effects related to subband non-parabolicity and to the momentum-dependence of the dipole matrix elements, which for p-type structures operating at room temperature (RT) are expected to play a relevant role, have been taken into account. Sampling the Brillouin zone around the Γ point we have also calculated, relying on the approach described in [32], the absorption spectra for different values of the applied electrical bias.

For the sake of clarity, we will first analyze the electronic structure and the absorption spectrum of the two heterostructures in the absence of external electrical field (EF) at RT and at T = 4K (LT). We begin our discussion noticing that in the MIR, both intersubband transitions and free carrier absorption contributes to the absorbance. However, only the first mechanism can guarantee a significant electro-optical effect, since the spectral shape of the free carrier absorption is quite bias independent. Therefore, in order to maximize the IST features in the absorption spectrum, we designed our single mode waveguides to support a TM polarized field. In fact, the IST features in the absorption spectrum are enhanced when the polarization vector is oriented parallel to the growth direction [33–37]. For the adopted doping density, LT and up to RT, holes mainly populate the fundamental subband which, in our compressively strained quantum wells, originates from the heavy hole band (HH). It follows that with TM polarized light, the dominant ISB absorption peaks are due to transition from H_0 to excited subband with the same orbital symmetry, while transitions with LH subbands as final state, which are dominant in vertically illuminated devices, give only a minor contribution in our waveguide devices [33,35,37].

The Γ-point band edge potential energy profiles for the HH and LH bands of the StQW are reported in Fig. 2(c), setting the reference energy to have the ground state H_0 at 0 eV. The heterostructure features three confined HH subbands: the ground state H_0, tightly confined in the deeper well and the excited H_1 (-0.157 eV) and H_2 (-0.19 eV) levels which extend also in the step well. As a consequence, the symmetry selection rule which for square QW systems suppresses the $H_0 \rightarrow H_2$ transition for TM light does not apply in our case and then both the $H_0 \rightarrow H_1$ and the $H_0 \rightarrow H_2$ ISBs are active. In line with the above considerations, we find that at LT the ISB contribution to the optical absorption spectrum α_{QW} features two main peaks, located at $\lambda = 7.75$ μm and $\lambda = 6.6$ μm, originating from the $H_0 \rightarrow H_1$ and the $H_0 \rightarrow H_2$ OT, respectively. The former one is accompanied by a low energy secondary peak located at $\lambda = 8.5$ μm, which we attribute to $H_0 \rightarrow L_1$ transitions. At RT, instead, the $H_0 \rightarrow H_1$ and $H_0 \rightarrow H_2$ transitions merge, originating an extended absorption band which covers the [5–9] μm interval. This effect is caused by the band

non-parabolicity (NP) which is apparent in the electronic structure shown in Fig. 2(a), due to the thermal excitation of H_0 holes with large in-plane momentum.
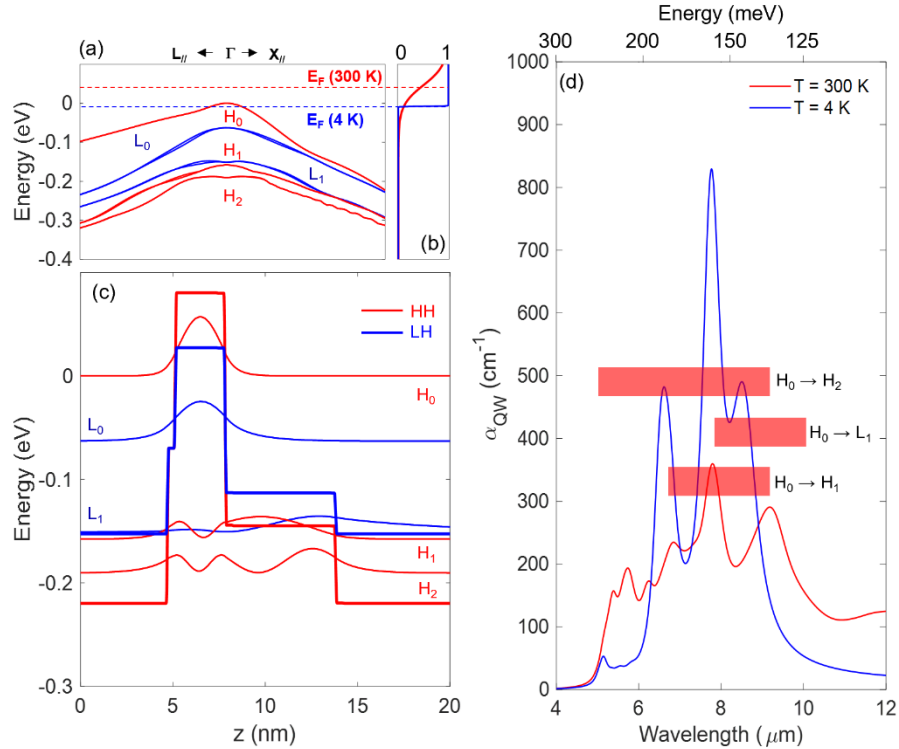
Fig. 2. Band-structure in a neighbor of the Γ point of the StQW (a). Fermi-Dirac distribution function at RT (red) and at LT (blue) for holes. Potential energy profiles for the HH (red) and LH (blue) bands, together with hole wavefunctions calculated at the Γ -point (c) The discontinuity of the energy profile seen at $z = 5$ nm is an artifact due to the discretization step related to the (finite monolayer spacing) atomistic character of the model. ISB contribution α_{QW} to the absorption spectrum as a function of the wavelength at RT (red) and at LT (blue) for the StQW. Red boxes highlight the energy ranges at RT of the main ISBs (d).

As a matter of fact, at RT the tail of the Fermi distribution extends down to $E_F-k_BT = -0.064$ eV (see Fig. 3(b). Taking into account this value, we have reported in Fig. 2(d), using red boxes the spectral range associated to the $H_0 \rightarrow H_1$, $H_0 \rightarrow H_2$ and $H_0 \rightarrow L_1$ transitions which are active at RT. The large overlap of the these two spectral ranges justifies the observed temperature induced merging of the two peaks.

Similar considerations hold also for the TQW design. Its band edge profile, calculated at the VB maximum for the HH and LH bands is reported in Fig. 3(c). Also in this case, the heterostructure features three HH subbands: the ground state H_0, deeply confined at the bottom of the triangular well, and the H_1 and H_2 states which lie at -0.135 eV and -0.241 eV, respectively. At RT the Fermi level E_F is found at 0.046 eV and the ground state is populated down to $E_F-k_BT = -0.075$ eV (see panels a and b in Fig. 3), indicating that ISBs at large in-plane momentum k significantly contribute to the α_{QW} absorption spectrum (Fig. 3(d)). In line with this fact, we have attributed peak located at $\lambda = 9.3$ μm to the $H_0 \rightarrow H_1$ ISB. The spectral features at shorter wavelengths are due to the $H_0 \rightarrow H_2$ and to the $H_0 \rightarrow L_1$ which are partially overlapped at RT. In conclusion, as for the StQW structure, the optical absorption spectrum of TQW is dominated by the $H_0 \rightarrow H_1$,
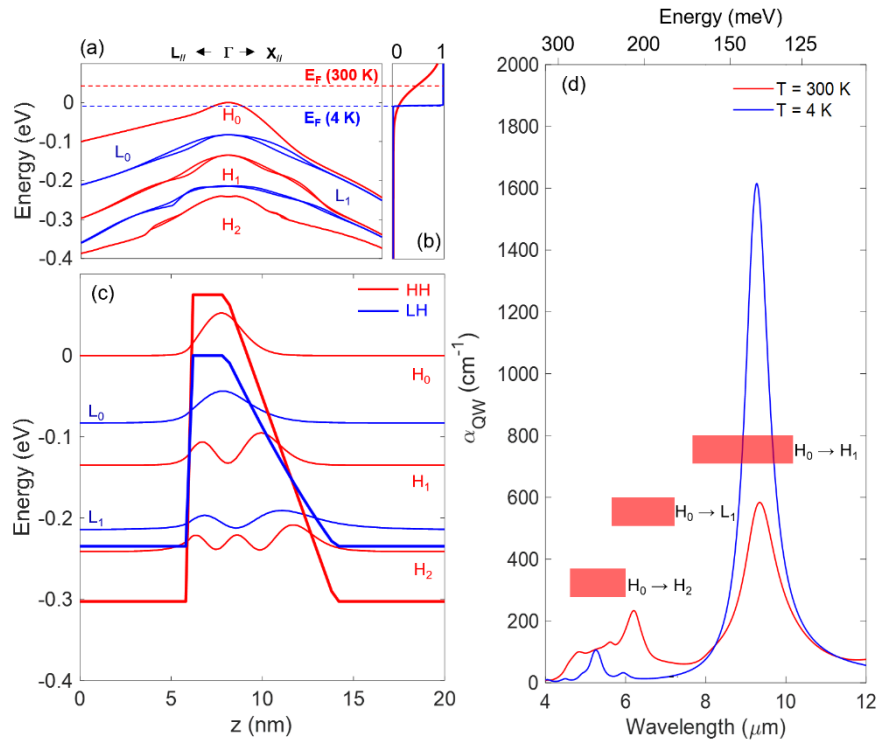
Fig. 3. Band-structure in a neighbor of the Γ point of the TQW (a). Fermi-Dirac distribution function at RT (red) and at LT (blue) for holes. Potential energy profiles for the HH (red) and LH (blue) bands, together with hole wavefunctions calculated at the Γ -point (c). ISB contribution α_{QW} to the absorption spectrum as a function of the wavelength at RT (red) and at LT (blue) for the StQW. Red boxes highlight the energy ranges at RT of the main ISBs (d).

$H_0 \rightarrow H_2$ and $H_0 \rightarrow L_1$ features, with minor contributions which can be attributed to the presence of more excited HH subbands.
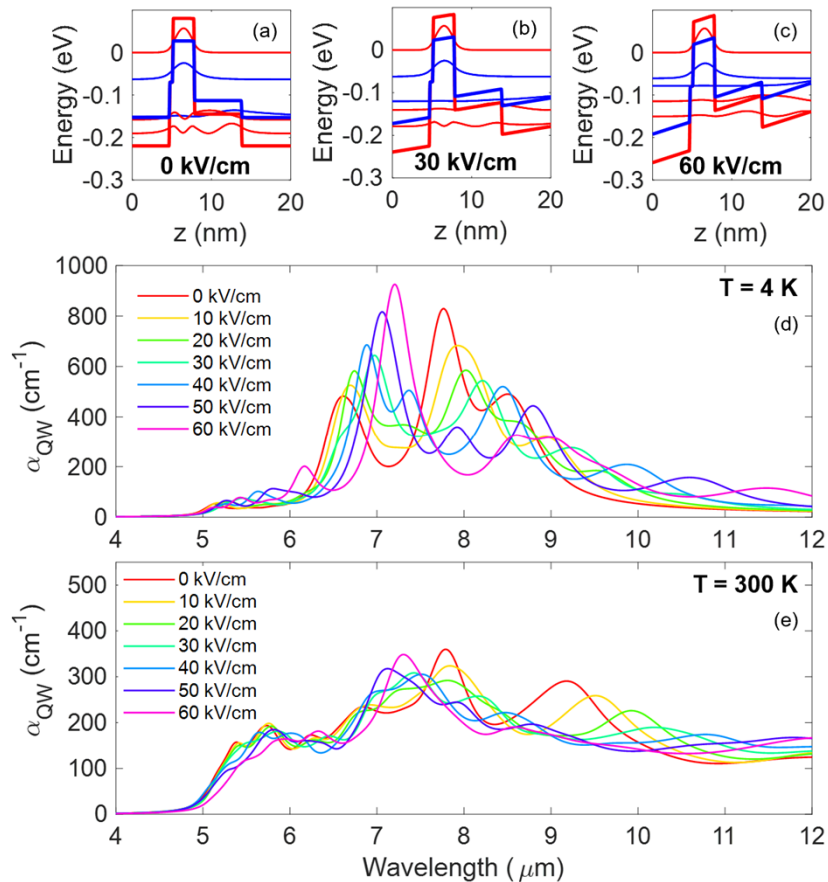
Electronic structure and absorption spectrum with an external electric field

The electronic spectrum, calculated at the Γ point at different EF for the StQW system is reported in Fig. 4 a – c. Upon increasing the EF, the potential confinement experienced by the H_1 and H_2 states become progressively less effective since the band bending induced by the electric field facilitates the leaking of their wavefunctions in the right barrier. Consequently, the $H_0 \rightarrow H_1$ and $H_0 \rightarrow H_2$ energy separation decreases. This effect is the main responsible for the variation in the absorption spectrum at LT clearly visible in Fig. 4(d) where $\alpha_{QW}(\lambda)$ has been calculated for different values of the EF, varying in the 0-60 kV/cm interval. Indeed, upon increasing the EF the two main peaks experience a significant red-shift which we relate to the reduction of the energy difference between the excited H subbands and the H_0 one. It follows that the electrical bias triggers a significant decrease of the peak value of the absorption at the wavelength associated to unbiased $H_0 \rightarrow H_2$ ISB. More precisely, at $\lambda = 6.6$ μm the application of a 60 kV/cm bias reduces the absorption from 484 to 113 cm^{-1}. A comparable suppression is expected to occur also in a spectral neighbour of $\lambda = 7.75$ μm due to the redshift of the $H_0 \rightarrow H_1$ peak. At RT, due to the significant overlap between the $H_0 \rightarrow H_1$ and $H_0 \rightarrow H_2$ OT discussed previously, the details of the evolution of the spectrum become rather complex. A strong red-shift of the peak located at

$\lambda = 9.2\ \mu m$ is clearly observable. It follows for instance that the application of an electric field of 60 kV/cm decreases the absorption at $\lambda = 9.2\ \mu m$ from 290 to 165 cm^{-1} due to the redshift of the $H_0 \rightarrow H_1$.

The same kind of analysis can be repeated for the TQW, whose spectrum, characterized by better resolved $H_0 \rightarrow H_1$ and $H_0 \rightarrow H_2$ and $H_0 \rightarrow L_1$ features, exhibits modulation effects of comparable magnitude. The electronic structure of the VB at the Γ point at different EF for the TQW are reported in Fig. 5 a,b,c. Also in this case, for increasing EF the potential confinement experienced by the H_1 and H_2 states become less effective, although the respective wavefunctions in the explored bias range remain fully confined in the potential well. Their energy difference with respect to the ground state is continuously reduced upon increasing the field and thus both the $H_0 \rightarrow H_1$ and $H_0 \rightarrow H_2$ peaks in the α_{QW} absorption spectrum experience a redshift (see Fig. 5(d)). However, in this case we do not observe a significant variation in the peak intensities since the field induced redistribution of the wavefunction spatial density, which affect the oscillator strengths, is now more modest.

To make a quantitative comparison with the StQW design, we estimate that the application of an electric field of 60 kV/cm triggers a suppression of the RT absorption coefficient at the $H_0 \rightarrow H_1$ at $\lambda = 9.9\ \mu m$ from the value of 570 cm^{-1} down to 280 cm^{-1}.

Fig. 4. Electronic structure of the StQW at the VB maximum with EF of 0 kV/cm (a), 30 kV/cm (b) and 60(c) kV/cm. Absorption spectra of StQW as a function of the wavelengths for different intensities of the EF at LT (d) and at RT (e).
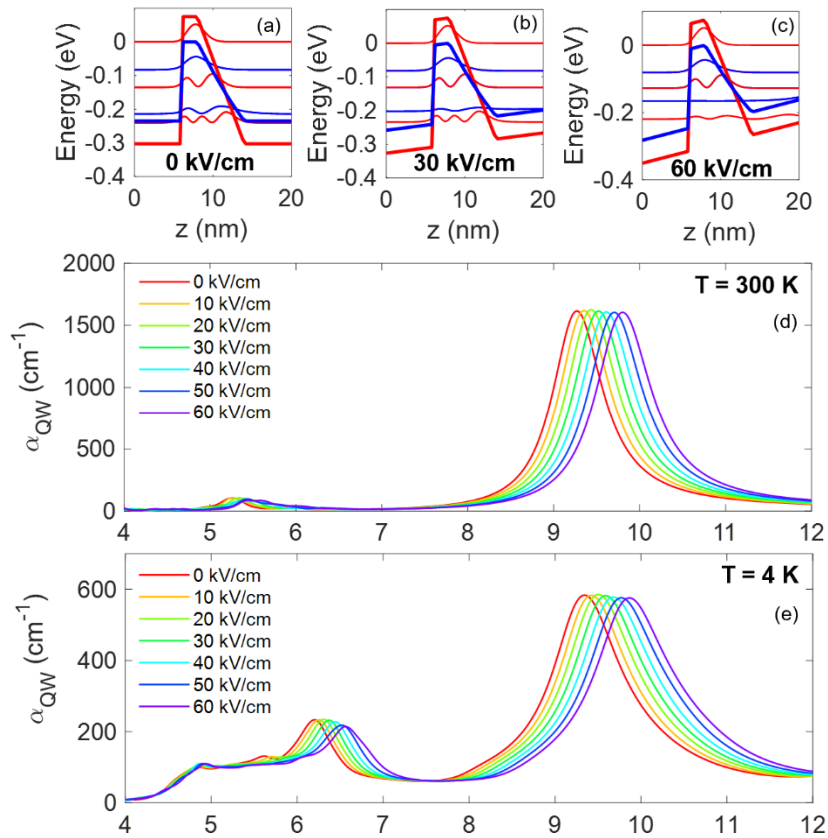
Fig. 5. Electronic structure of the TQW at the VB maximum with EF of 0 kV/cm (a), 30 kV/cm (b) and 60(c) kV/cm. Absorption spectra of TQW as a function of the wavelengths for different intensities of the external EF at LT (d) and at RT (e).

Waveguide integration and modulator performances

WG integration of Ge/SiGe QWs requires a SiGe buffer material that could serve as a fully relaxed VS to allow the growth of high quality QWs and at the same time as waveguiding layer. Such challenge has already been successfully addressed to realize WG integrated intensity modulator at telecom wavelengths [24] through the use of few μm thick SiGe linear graded buffers (GB) deposited on Si. This approach is even more advantageous at LWIR wavelengths, since the linear increase of the refractive index toward the Ge-rich part of the structure helps to confine the optical mode far from the Si substrate, which become lossy beyond $\lambda = 8$ μm [38].

In order to study the modulation performances of the LWIR devices here investigated, we propose the rib WG structures reported in Fig. 6, which have been designed for single mode operation between $\lambda = 5$ μm and $\lambda = 12$ μm. The WG structure for the StQW (TQW) consist in a linearly graded $Si_{1-y}Ge_y$ buffer where the Ge concentration y is raised from 0 to 79% (69%) with a grading rate of 7%/μm. The GB is followed by a 2 μm thick $Si_{0.2}Ge_{0.8}$ ($Si_{0.3}Ge_{0.7}$) constant composition layer, which serves as a VS for the QWs. The final 150 nm of the VS are p-doped ($Na = 1 \times 10^{18}$ cm^{-3}) to form the bottom contact layer. The WG core consists in 220 (160) repetitions of the StQW (TQW) period, for a total thickness of 2 μm, followed by a 200 nm thick layer with the same composition of the VS. The final 100 nm of such layer are p-doped ($Na = 1 \times 10^{18}$ cm^{-3}) to fabricate the top contact. To assess the overlap between the optical mode

and the individual layers the intensity of the electric field of the fundamental optical mode in TM polarization between $\lambda = 4$ μm and $\lambda = 12$ μm have been calculated using the finite difference method, as implemented in the package MODE of the Lumerical software platform. The results at $\lambda = 10$ μm are reported in Fig. 6.
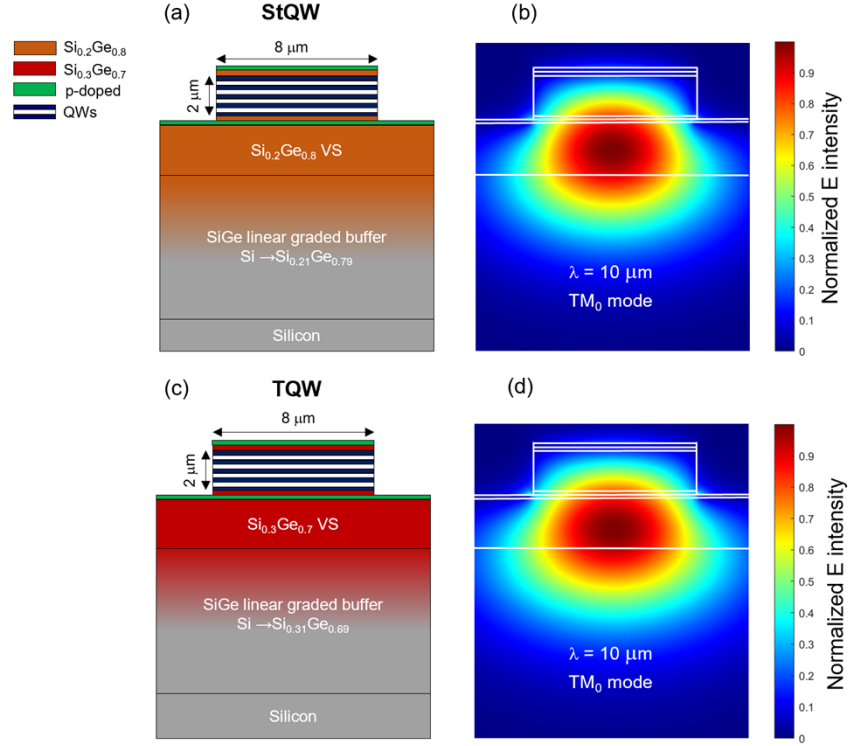
Fig. 6. Epitaxial structure and geometrical shape of the proposed WG for the StQW (a) and the TQW (b). Panel (b) and (d) represent the corresponding normalized E-field intensity at $\lambda = 10$ μm for the fundamental TM mode.

The modulation performances have been evaluated in terms of the extinction ratio (ER), the insertion loss (IL) and the cut-off frequency. The ER as a function of the applied bias voltage V and wavelength λ is calculated according to:

$$ER(V, \lambda) = 10\log_{10}\left(\frac{P(0, \lambda)}{P(V, \lambda)}\right) \tag{1}$$

where P(V,λ) is the transmitted optical power at wavelength λ and voltage *V*. P(V,λ) can be expressed as:

$$P(V, \lambda) = P_{in} \exp(-\alpha_{QW}(V, \lambda) \cdot \Gamma_{QW}(\lambda) \cdot L - \alpha_{FCA}(\lambda) \cdot \Gamma_{QW,p}(\lambda) \cdot L$$
$$-\alpha_{FCA}(\lambda) \cdot \Gamma_p(\lambda) \cdot L) \tag{2}$$

where P_{in} is the input power at the entrance of the waveguide of length L and α_{QW} and α_{FCA} are the ISB and the free carrier absorption (FCA), respectively. Accordingly, in eq.(1) Γ_{QW}, $\Gamma_{QW,p}$ and Γ_p represent the overlap of the optical mode with the QW region, the p-doped layers in the wells, and the contacts. Notice that in the above expression the only bias dependent quantity is α_{QW}.

The FCA contributions in the well and contact regions have been both modelled using the equation [39]:

$$\alpha_{FCA}(\lambda) = c(\lambda) \cdot N_a{}^{d(\lambda)} \tag{3}$$

The wavelength-dependent coefficients c(λ) and d(λ) have been taken from the experimental data available for Ge [39] and Si [40] and have been linearly interpolated with the Ge concentration to estimate the appropriate $Si_{1-y}Ge_y$ values. In these calculations, FCA in the QWs have been treated as for bulk material, due to the lack of experimental data about 2D FCA in Ge/SiGe QWs.

Finally, the total IL have been calculated as:

$$IL(\lambda) = 10\log_{10}\left(\frac{P_{in}}{P_{\max}}\right) \tag{4}$$

With $P_{\max}$ is the maximum optical power transmitted by the device. The propagation losses, typically falls into the 2-3 dB/cm [22] range for undoped Ge-rich SiGe WGs, have been neglected in the calculations. The ER per unit length of StQW and TQW is plotted in Fig. 7 a and b respectively. The StQW can be used for intensity modulation around λ = 7.3 μm, with a maximum ER per unit length of 8.5×10^{-3} dB/μm with an applied electric field of 60 kV/cm. By looking at Fig. 7(c), it can be noted that an ER of 1 dB can be reached with a 120 μm long device, with an associated IL of 2.5 dB. The TQW exhibit interesting modulation performances at λ = 6.6 μm and at λ = 10 μm, where it shows a maximum ER per unit length of 12×10^{-3} dB/μm at the highest electric filed considered. In this case, in order to achieve and ER of 1 dB at λ = 10 μm, a device length of 80 μm is required, with an associated IL of 1.5 dB.
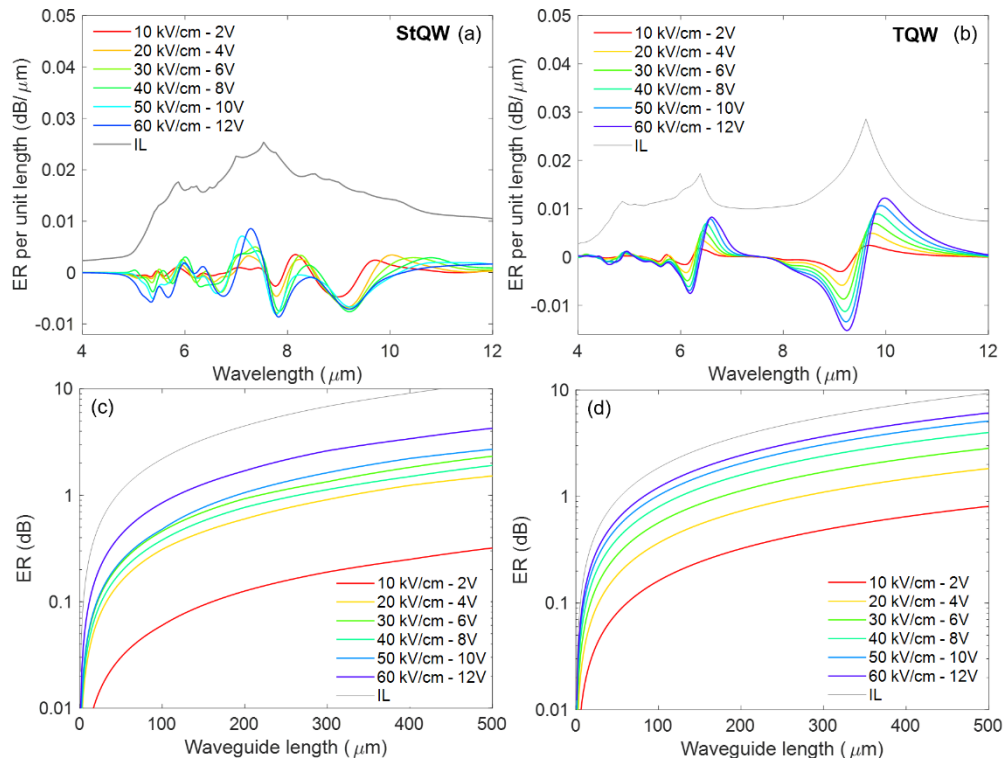

Fig. 7. Specific ER and IL as a function of the wavelength of the StQW and the TQW at different bias voltages (a and b). ER and IL as a function of the WG length at different bias voltages for the StQW at λ = 6.6 μm (c) and for the TQW at λ = 10 μm (d).

Frequency response

The dynamic behavior of quantum-well based devices is usually determined by two main parameters: the RC time constant, which is mainly determined by the geometry of the device, and the escape time τ of the photoexcited carriers from the potential well, which is controlled by the potential profile and by intrinsic material properties. Since here we are considering only optical modulation and not photodetection, the speed of the device is not limited by the escape time, which can be safely neglected in the calculation, at least considering input intensities well below the saturation, which normally occurs around $10\,\mathrm{MW/cm^2}$ [41]. By following the analysis performed in [42], we can model the QW device by a parallel resistance-capacitance (RC) equivalent circuit, where C is the device capacitance, which can be calculated in a parallel-plate capacitor approximation and $R = R_L = 50\,\Omega$ is the load-resistance of the circuit. The maximum cut-off frequency can then be calculated as:

$$f_{RC} = \frac{1}{2\pi R_L C} \tag{5}$$

The cut-off frequency $f_{cut-off}$ as a function of the modulator length, is reported in Fig. 8 and it is valid for both the StQW and TQW heterostructure. Here we have to point out that the model used to calculate $f_{cut-off}$ is rather simple and the results should be confirmed experimentally. Nevertheless, high-speed quantum wells infrared photodetectors with $f_{cut-off}$ of several tens of GHz and similar device areas have been reported in the literature [42,43].
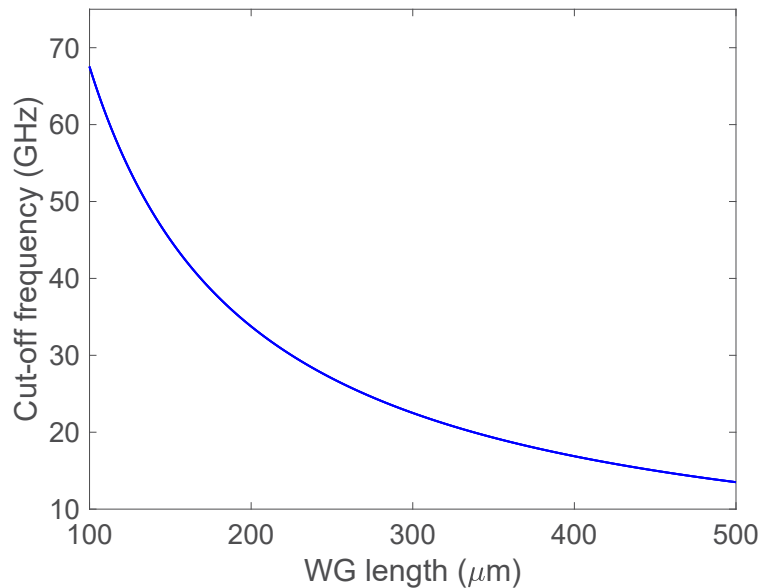
Fig. 8. Cut-off frequency as a function of the WG length, as calculated with Eq. (6).

Conclusions

In this work, we have theoretically investigated the possibility to obtain high-speed modulation at mid-infrared frequencies by exploiting the QCSE in waveguide integrated Ge/SiGe asymmetric QWs. Thanks to the strength of the QCSE, the investigated heterostructures could provide ERs exceeding 1 dB while maintaining a very small footprint with respect to EOM based on FCPD, which typically need mm-long WGs to achieve similar ER levels. Our calculations show that,

thanks to such small footprint, modulation speed of several tens of GHz could be achievable. Such performances could be further improved by optimizing the QW design as well as the WG geometry for specific wavelengths.

Disclosures. The authors declare no conflicts of interest.

Data availability. Data underlying the results presented in this paper are not publicly available at this time but may be obtained from the authors upon reasonable request.

References

1. V. Mittal, M. Nedeljkovic, L. G. Carpenter, A. Z. Khokhar, H. M. H. Chong, G. Z. Mashanovich, P. N. Bartlett, and J. S. Wilkinson, "Waveguide Absorption Spectroscopy of Bovine Serum Albumin in the Mid-Infrared Fingerprint Region," ACS Sens. **4**(7), 1749–1753 (2019).
2. M. Yu, Y. Okawachi, A. G. Griffith, M. Lipson, and A. L. Gaeta, "Microfluidic mid-infrared spectroscopy via microresonator-based dual-comb source," Opt. Lett. **44**(17), 4259–4262 (2019).
3. A. Vasiliev, A. Malik, M. Muneeb, B. Kuyken, R. Baets, and G. Roelkens, "On-Chip Mid-Infrared Photothermal Spectroscopy Using Suspended Silicon-on-Insulator Microring Resonators," ACS Sens. **1**(11), 1301–1307 (2016).
4. Y.-C. Chang, P. Wägli, V. Paeder, A. Homsy, L. Hvozdara, P. van der Wal, J. Di Francesco, N. F. de Rooij, and H. Peter Herzig, "Cocaine detection by a mid-infrared waveguide integrated with a microfluidic chip," Lab Chip **12**(17), 3020–3023 (2012).
5. B. G. Lee, M. A. Belkin, R. Audet, J. MacArthur, L. Diehl, C. Pflügl, F. Capasso, D. C. Oakley, D. Chapman, A. Napoleone, D. Bour, S. Corzine, G. Höfler, and J. Faist, "Widely tunable single-mode quantum cascade laser source for mid-infrared spectroscopy," Appl. Phys. Lett. **91**(23), 231101 (2007).
6. P. T. Lin, S.W. Kwok, H.Y.G. Lin, V. Singh, L.C. Kimerling, G.M. Whitesides, and A. Agarwal, "Mid-Infrared spectrometer using opto-nanofluidic slot-waveguide for label-free on-chip chemical sensing," Nano Letters **14**,231–238 (2014).
7. M. L. Meade, "Advances in lock-in amplifiers," J. Phys. E: Sci. Instrum. **15**(4), 395–403 (1982).
8. H. Lin, Z. Luo, T. Gu, L. C. Kimerling, K. Wada, A. Agarwal, and J. Hu, "Mid-infrared integrated photonics on silicon: a perspective," Nanophotonics **7**(2), 393–420 (2017).
9. R. Soref, "Mid-infrared photonics in silicon and germanium," Nat. Photonics **4**(8), 495–497 (2010).
10. Y. Su, W. Wang, X. Hu, H. Hu, X. Huang, Y. Wang, J. Si, X. Xie, B. Han, H. Feng, Q. Hao, G. Zhu, T. Duan, and W. Zhao, "Gbps DPSK transmission over free-space link in the mid-infrared," Opt. Express **26**(26), 34515–34528 (2018).
11. M. Nedeljkovic, C. Littlejohns, A. Khokhar, M. Banakar, W. Cao, J. Penades, D. Tran, F. Gardes, D. Thomson, G. Reed, H. Wang, and G. Mashanovich, "Silicon-on-insulator free-carrier injection modulators for the mid-infrared," Opt. Lett. **44**(4), 915–918 (2019).
12. G. Mashanovich, M. Nedeljkovic, J. Soler-Penades, Z. Qu, W. Cao, A. Osman, Y. Wu, C. Stirling, Y. Qi, Y. Cheng, L. Reid, C. Littlejohns, J. Kang, Z. Zhao, M. Takenaka, T. Li, Z. Zhou, F. Gardes, D. Thomson, and G. Reed, "Group IV mid-infrared photonics [Invited]," Opt. Mater. Express **8**(8), 2276–2286 (2018).
13. D. Marris-Morini, V. Vakarin, J. M. Ramirez, Q. Liu, A. Ballabio, J. Frigerio, M. Montesinos, C. Alonso-Ramos, X. Le Roux, S. Serna, D. Benedikovic, D. Chrastina, L. Vivien, and G. Isella, "Germanium-based integrated photonics from near- to mid-infrared applications," Nanophotonics **7**(11), 1781–1793 (2018).
14. L. Zhang, A. Agarwal, L. C. Kimerling, and J. Michel, "Nonlinear Group IV photonics based on silicon and germanium: from near-infrared to mid-infrared," Nanophotonics **3**(4-5), 247–268 (2014).
15. V. Mittal, G. Devitt, M. Nedeljkovic, L. Carpenter, H. Chong, J. Wilkinson, S. Mahajan, and G. Mashanovich, "Ge on Si waveguide mid-infrared absorption spectroscopy of proteins and their aggregates," Biomed. Opt. Express **11**(8), 4714–4722 (2020).
16. D. Kozak, N. Tyndall, M. Pruessner, W. Rabinovich, and T. Stievater, "Germanium-on-silicon waveguides for long-wave integrated photonics: ring resonance and thermo-optics," Opt. Express **29**(10), 15443–15451 (2021).
17. M. Sinobad, C. Monat, B. Luther-Davies, P. Ma, S. Madden, D. Moss, A. Mitchell, D. Allioux, R. Orobtchouk, S. Boutami, J. Hartmann, J. Fedeli, and C. Grillet, "Mid-infrared octave spanning supercontinuum generation to 8.5 µm in silicon-germanium waveguides," Optica **5**(4), 360–366 (2018).
18. M. Montesinos-Ballester, Q. Liu, V. Vakarin, J. M. Ramirez, C. Alonso-Ramos, X. Le Roux, J. Frigerio, A. Ballabio, E. Talamas, L. Vivien, G. Isella, and D. Marris-Morini, "On-chip Fourier-transform spectrometer based on spatial heterodyning tuned by thermo-optic effect," Sci. Rep. **9**(1), 14633 (2019).
19. C. Ho, Z. Zhao, Q. Li, S. Takagi, and M. Takenaka, "Mid-infrared tunable Vernier filter on a germanium-on-insulator photonic platform," Opt. Lett. **44**(11), 2779–2782 (2019).
20. A. Sánchez-Postigo, A. Ortega-Moñux, J. Soler Penadés, A. Osman, M. Nedeljkovic, Z. Qu, Y. Wu, Í Molina-Fernández, P. Cheben, G. Mashanovich, and J. Wangüemert-Pérez, "Suspended germanium waveguides with subwavelength-grating metamaterial cladding for the mid-infrared band," Opt. Express **29**(11), 16867–16878 (2021).

21. T. Li, M. Nedeljkovic, N. Hattasan, W. Cao, Z. Qu, C. Littlejohns, J. Penades, L. Mastronardi, V. Mittal, D. Benedikovic, D. Thomson, F. Gardes, H. Wu, Z. Zhou, and G. Mashanovich, "Ge-on-Si modulators operating at mid-infrared wavelengths up to 8 µm," Photonics Res. **7**(8), 828–836 (2019).

22. M. Montesinos-Ballester, L. Deniel, N. Koompai, T. H. N. Nguyen, J. Frigerio, A. Ballabio, V. Falcone, X. Le Roux, C. Alonso-Ramos, L. Vivien, A. Bousseksou, G. Isella, and D. Marris-Morini, "Mid-infrared Integrated Electro-optic Modulator Operating up to 225 MHz between 6.4 and 10.7 µm Wavelength," ACS Photonics **9**(1), 249–255 (2022).

23. M. Montesinos-Ballester, V. Vakarin, J. M. Ramirez, Q. Liu, C. Alonso-Ramos, X. Le Roux, J. Frigerio, A. Ballabio, A. Barzaghi, L. Deniel, D. Bouville, L. Vivien, G. Isella, and D. Marris-Morini, "Optical modulation in Ge-rich SiGe waveguides in the mid-infrared wavelength range up to 11 µm," Commun. Mater. **1**(1), 6 (2020).

24. R. A. Griffin, S. K. Jones, N. Withbread, S. C. Heck, and L. N. Langley, "InP Mach-Zehnder modulator platform for 10/40/100/200 Gb/s operation," IEEE J. Select. Topics Quantum Electron. **19**(6), 158–166 (2013).

25. P. Chaisakul, D. Marris-Morini, J. Frigerio, D. Chrastina, M.-S. Rouifed, S. Cecchi, P. Crozat, G. Isella, and L. Vivien, "Integrated germanium optical interconnects on silicon substrates," Nat. Photonics **8**(6), 482–488 (2014).

26. S. Pirotta, N. L. Tran, A. Jollivet, G. Biasiol, P. Crozat, J.-M. Manceau, A. Bousseksou, and R. Colombelli, "Fast amplitude modulation up to 1.5 GHz of mid-IR free-space beams at room temperature," Nat. Commun. **12**(1), 799 (2021).

27. K. Gallacher, A. Ballabio, R. W. Millar, J. Frigerio, A. Bashir, I. MacLaren, G. Isella, M. Ortolani, and D. J. Paul, "Mid-infrared intersubband absorption from p-Ge quantum wells grown on Si substrates," Appl. Phys. Lett. **108**(9), 091114 (2016).

28. J. Aberl, M. Brehm, T. Fromherz, J. Schuster, J. Frigerio, and P. Rauter, "SiGe quantum well infrared photodetector s on strained silicon-on-insulator," Opt. Express **27**(22), 32009 (2019).

29. J. Frigerio, A. Ballabio, M. Ortolani, and M. Virgilio, "Modeling of second harmonic generation in hole-doped silicon-germanium quantum wells for mid-infrared sensing," Opt. Express **26**(24), 31861–31872 (2018).

30. J. Frigerio, C. Ciano, J. Kuttruff, A. Mancini, A. Ballabio, D. Chrastina, V. Falcone, M. De Seta, L. Baldassarre, J. Allerbeck, D. Brida, L. Zeng, E. Olsson, M. Virgilio, and M. Ortolani, "Second Harmonic Generation in Germanium Quantum Wells for Nonlinear Silicon Photonics," ACS Photonics **8**(12), 3573–3582 (2021).

31. A. Ballabio, J. Frigerio, S. Firoozabadi, D. Chrastina, A. Beyer, K. Volz, and G. Isella, "Ge/SiGe parabolic quantum wells," J. Phys. D: Appl. Phys. **52**(41), 415105 (2019).

32. M. Virgilio and G. Grosso, "Valence and conduction intersubband transitions in SiGe, Ge-rich, quantum wells on [001] Si$_{0.5}$Ge$_{0.5}$ substrates: A tight-binding approach," J. Appl. Phys. **100**(9), 093506 (2006).

33. M. Virgilio and G. Grosso, "Valley splitting and optical intersubband transitions at parallel and normal incidence in [001]-Ge/SiGe quantum wells," Phys. Rev. B **79**(16), 165310 (2009).

34. A. A. Bloshkin, "Interlevel optical transitions in Si/Ge$_x$Si$_{1-x}$/Si quantum wells," Optoelectron. Instrument. Proc. **50**(3), 252–259 (2014).

35. J. M. Berroir, S. Zanier, Y. Guldner, J. P. Vieren, I. Sagnes, Y. Campidelli, and P. A. Badoz, "Infrared spectroscopy in p-type SiGe/Si quantum wells," Appl. Surf. Sci. **102**, 331–335 (1996).

36. S. Zanier, Y. Guldner, J.M. Berroir, J.P. Vieren, I. Sagnes, Y. Campidelli, and P.A. Badoz, "Infrared absorption in p-type SiGeSi quantum wells: Intersubband transition and free carrier contributions," Solid-State Electron. **40**(1-8), 123–126 (1996).

37. T. Fromherz, E. Koppensteiner, M. Helm, G. Bauer, J. F. Nützel, and G. Abstreiter, "Hole energy levels and intersubband absorption in modulation-doped Si/Si$_{1-x}$Ge$_x$ multiple quantum wells," Phys. Rev. B **50**(20), 15073–15085 (1994).

38. J. M. Ramirez , Q. Liu, V. Vakarin, J. Frigerio, A. Ballabio, X. Le Roux, D. Bouville, L. Vivien, G. Isella, and D. Marris-Morini, "Graded SiGe waveguides with broadband low-loss propagation in the mid infrared," Opt. Express **26**(2), 870–877 (2018).

39. R. A. Soref and B. R. Bennet, "Electrooptical effects in Silicon," IEEE J. Quantum Electron. **23**(1), 123–129 (1987).

40. M. Nedeljkovic, R. Soref, and G. Z. Mashanovich, "Predictions of Free-Carrier Electroabsorption and Electrorefraction in Germanium," IEEE Photonics J. **7**(3), 1–14 (2015).

41. M. Nedeljkovic, R. Soref, and G. Z. Mashanovich, "Free-carrier electrorefraction and electroabsorption modulation predictions for silicon over the 1.3–14 um infrared wavelength range," IEEE Photonics J. **3**(6), 1171–1180 (2011).

42. R. Steed, M. Matthews, J. Plumridge, M. Frogley, C. Phillips, Z. Ikonic, P. Harrison, O. Malis, L. N. Pfeiffer, and K. W. West, "Saturation of intersubband transitions in p-doped GaAs /AlGaAs quantum wells," Appl. Phys. Lett. **92**(18), 183104 (2008).

43. H. C. Liu, J. Li, M. Buchanan, and Z. R. Wasilewslu, "High-Frequency Quantum-Well Infrared Photodetectors Measured by Microwave-Rectification Technique," IEEE J. Quantum Electron. **32**(6), 1024–1028 (1996).

44. H. C. Liu, G. R. Jenkins, E. R. Brown, K. A. McIntosh, K. B. Nichols, and M. J. Manfra, "Optical Heterodyne Detection and Microwave Rectification Up to 26 GHz Using Quantum Well Infrared Photodetectors," IEEE Electron. Device Lett. **16**(6), 253–255 (1995).